Available online at www.sciencedirect.com
SCIENCE DIRECT®
Journal of Molecular Spectroscopy 235 (2006) 1–17
Journal of MOLECULAR SPECTROSCOPY
www.elsevier.com/locate/jms

The A^2B_2–X^2A_1 electronic transition of $^{15}NO_2$: A rovibronic survey covering 14 300–18 000 cm^{-1}

E.A. Volkers [a], M.C. Koudijzer [a], A. Vredenborg [a], J. Bulthuis [a], S. Stolte [a], H. Linnartz [a,b,*], R. Jost [c]

[a] Department of Physical Chemistry, Laser Centre Vrije Universiteit, De Boelelaan 1083, NL 1081 HV Amsterdam, The Netherlands
[b] Sackler Laboratory for Astrophysics, Leiden Observatory, Postbus 9513, NL 2300 RA Leiden, The Netherlands
[c] Laboratoire de Spectrométrie Physique, Université Joseph Fourier de Grenoble, BP 87, F38402 Saint Martin d'Hères Cedex, France

Received 26 July 2005; in revised form 19 September 2005
Available online 10 November 2005

Abstract

More than 250 rotationally resolved vibrational bands of the A^2B_2–X^2A_1 electronic transition of $^{15}NO_2$ have been observed in the 14 300–18 000 cm^{-1} range. The bands have been recorded in a recently constructed setup designed for high resolution spectroscopy of jet cooled molecules by combining time gated fluorescence spectroscopy and molecular beam techniques. The majority of the observed bands has been rotationally assigned and can be identified as transitions starting from the vibrational ground state or from vibrationally excited (hot band) states. An exceptionally strong band is located at 14 851 cm^{-1} and studied in more detail as a typical benchmark transition to monitor $^{15}NO_2$ in atmospheric remote sensing experiments. Standard rotational fit routines provide band origins, rotational and spin rotation constants. A subset of 177 vibronic levels of $^2B_2$ vibronic symmetry has been analyzed in the energy range between 14 300 and 17 250 cm^{-1}, in terms of integrated density and using Next Neighbor Distribution. It is found that the overall statistical properties and polyad structure of $^{15}NO_2$ are comparable to those of $^{14}NO_2$ but that the internal structures of the polyads are completely different. This is a direct consequence of the X^2A_1–A^2B_2 vibronic mixing.

Keywords: High resolution spectroscopy; Electronic spectroscopy; NO_2 isotopologues; $^{15}NO_2$; Spectroscopic survey

1. Introduction

In the last decade much efforts have been made to interpret high resolution data of the A^2B_2–X^2A_1 electronic spectrum of $^{14}N^{16}O_2$ [1–13]. This spectrum is very dense, even though NO_2 is a small near-prolate asymmetric rotor. The origin of the spectral congestion is found in the strong vibronic coupling between the X^2A_1 ground state and the lowest electronically excited A^2B_2 state via the anti-symmetric stretch coordinate of b_2 symmetry, taking place above the conical intersection of the two potential energy surfaces at a rather low energy of about 10 000 cm^{-1}. As a consequence, spectral features have been vibronically assigned only well below and close to the conical intersection. For higher energies identifications are rare: above 12 000 cm^{-1} vibrational assignments are ambiguous and above 16 500 cm^{-1} the nature of the spectra appears nearly vibronically chaotic.

In the case of other symmetric isotopologues like $^{15}N^{16}O_2$, a similar overall spectroscopic behavior is expected: a spectrum consisting of much more bands than expected for a simple tri-atomic molecule with an increasing complexity for higher energies. Rotational spacings and vibrational progressions will differ, reflecting minor differences in molecular masses. A tiny change in the vibrational frequencies and zero point energies (ZPE), however, induces a large change in the eigenstates mixing coefficients and in the relative intensity of the vibronic bands. Numerous

* Corresponding author. Fax: +31 71 5275819.
E-mail address: linnartz@strw.leidenuniv.nl (H. Linnartz).

0022-2852/$ - see front matter © 2005 Elsevier Inc. All rights reserved.
doi:10.1016/j.jms.2005.09.014

spectroscopic studies have been reported for the main isotopologue; $^{14}NO_2$. These comprise both cell [14] and cw or pulsed jet experiments, using direct absorption techniques—e.g., ICLAS [2,15], cavity ring down [16], bolometric [7,8], and LIF detection [17]. For the minor isotopologues of NO_2 much less spectroscopic information is available, mainly because of large gas consumption in these experiments and the high costs involved in studying ^{15}N or ^{18}O species. So far some infrared cell measurements have been reported [18–21] and spectroscopic observations in the visible range are largely lacking. The present work has been performed with a recently constructed spectroscopic setup optimized for minimal gas consumption, high sensitivity, and high spectral accuracy [22]. In this article more than 250 rovibronic bands of the A^2B_2–X^2A_1 electronic system of $^{15}NO_2$ are reported in the 555–700 nm range. All bands are rotationally resolved and the majority has been assigned. A number of benchmark transitions—among which a very strong transition around 14 851 cm^{-1}—is presented in detail. The excited state parameters of all observed bands are summarized in two overview tables and discussed in detail. A statistical comparison with data available for the corresponding $^{14}NO_2$ spectrum is presented as well.

2. Experiment

The experimental setup has been described in detail recently [22]. The second harmonic of a Nd:YAG laser is used to pump a tunable dye laser covering the frequency regime of 14 300–18 000 cm^{-1} (rhodamine 6G, sulforhodamine B, DCM, and pyridine 1) with a bandwidth of typically 0.07 cm^{-1}. In the 15 340–15 780 cm^{-1} region a larger linewidth of about 0.12 cm^{-1} has been found as a consequence of a change in the grating order. The laser beam is focused onto an expanding mixture of 1% $^{15}NO_2$ in Ar that is generated through a high intensity piezo electric pulsed molecular beam source that is optimized for a well-defined pulse shape during a short opening time of 150 μs. A gated photomultiplier tube is used to monitor the fluorescence zone that is about 1.5 cm downstream of the nozzle orifice. Typically 10 laser shots are averaged for each data point. An absolute frequency calibration with an accuracy better than 0.05 cm^{-1} is obtained by simultaneously recording an iodine absorption spectrum and/or the output of a wavemeter. As the setup has been designed for fully automatic scanning over large frequency ranges (typically segments of 150–200 cm^{-1}), an etalon signal with a FSR of 1.22 cm^{-1} is recorded to correct for non-linearities.

$^{15}NO_2$ is produced in a standard synthetic procedure from 99% pure $Na^{15}NO_3$ [23]. Sulfuric acid is added to sodium nitrate–^{15}N to produce nitric acid. The mixture is distilled to obtain the nitric acid–^{15}N product. The $H^{15}NO_3$ reacts with P_2O_5 (phosphorus (V) oxide) to produce nitrogen (V) oxide–^{15}N. When heated to 260 °C $^{15}N_2O_5$ dissociates into $^{15}NO_2$ and O_2. The final separation is obtained in a cold trap that is operated at 213 K. The purity of the gas obtained in this way has been checked by mass spectrometry and is better than 95%. For the frequency range presented here less than 0.5 g of $^{15}NO_2$ has been used.

3. Results

In Fig. 1 an intensity normalized stick diagram is shown that gives an overview of all recorded rovibronic bands in the A^2B_2–X^2A_1 electronic spectrum of $^{15}NO_2$

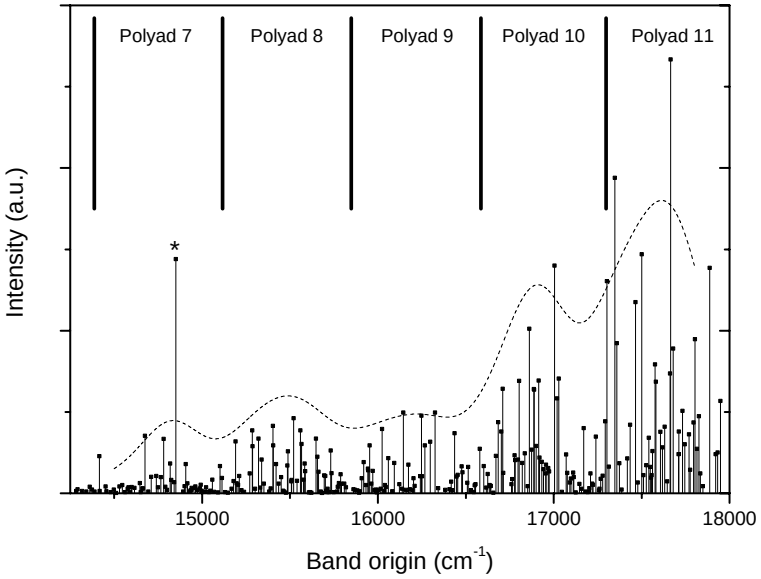

Fig. 1. A stick diagram representing the observed rovibronic bands within the A^2B_2–X^2A_1 electronic transition of $^{15}NO_2$. The overall intensity pattern is only indicative (see text) and visualizes a clear polyad structure. A single strong band at 14 851 cm^{-1} is indicated by an asterisk and is discussed in detail in Section 3.5.

in the 14 300–18 000 cm^{-1} region and that shows the complexity of the overall features. In total more than 250 separate rovibronic bands have been rotationally resolved. The overall intensity pattern shown in the figure exhibits a clear polyad structure and is obtained by adding individual bands that are represented by a Gaussian peak function with an intensity as listed in the tables and a width of 300 cm^{-1}. Furthermore, it is clear that for lower energy the intensity (and detection efficiency) decreases, whereas for higher energy spectral congestion increases.

Four different classes of rovibronic spectra are distinguished for the spectroscopic analysis and in the first part of this paper these bands are treated separately in an increasing order of complexity. Typical examples have been chosen to demonstrate spectral appearance and analysis. A summary of all molecular parameters of all observed bands is presented in two overview tables. The number of rotational transitions per band is limited because of the low final rotational temperature in the beam expansion, typically between 5 and 15 K. This prohibits in nearly all bands a determination of the effect of centrifugal distortion in the excited state. The vibrational temperature, however, is substantially higher and this is reflected in the appearance of hot band transitions. These start mainly from the excited bending state $(v_1, v_2, v_3) = (0,1,0)$ at 740 cm^{-1} [21] and in a few cases from $(0,2,0)$ at 1479 cm^{-1} or $(1,0,0)$ at 1306 cm^{-1} [24] and are unambiguously identified by determining differences in origin band positions and by comparing excited state rotational constants and spin splittings.

The center of a rotational transition is determined by fitting each individual line by a Gaussian function. The spectroscopic analysis has been performed using a non-linear least squares fit routine (Levenberg–Marquardt). To account for the rotational structure of the vibronic bands, we take three contributions to the Hamiltonian into account

$$H_{\mathrm{rot}} = H_{\mathrm{rigid}} + H_{\mathrm{SR}} + H_{\mathrm{cf}}. \tag{1}$$

Since NO_2 is a nearly symmetric top, the first contribution, the rigid rotor Hamiltonian, can be written as a series expansion in $(C-B)/(2A-B-C)$:

$$E = \nu_{\mathrm{bo}} + \frac{B+C}{2}N(N+1) + \left(A - \frac{B+C}{2}\right) \times \left(K^2 + C_1\left(\frac{C-B}{2A-B-C}\right) + C_2\left(\frac{C-B}{2A-B-C}\right)^2 + C_3\left(\frac{C-B}{2A-B-C}\right)^3\right), \tag{2}$$

where ν_{bo} indicates the band origin, A, B, and C are rotational constants, N is the rotational quantum number, K is the projection of N on the molecular a-axis, and C_1, C_2, and C_3 are constants defined in Appendix III of [25]. Accurate ground state constants are available from [20]: $A'' = 7.63077\ cm^{-1}$, $B'' = 0.43377\ cm^{-1}$, and $C'' = 0.40945\ cm^{-1}$. Rotational constants for hot band transitions starting from $(0,1,0)$ are available from [21]: $A''_{(010)} = 7.9843\ cm^{-1}$, $B''_{(010)} = 0.4337\ cm^{-1}$ and $C''_{(010)} = 0.4087\ cm^{-1}$. In the fit program the series expansion is carried to the third order. This is more than sufficient for the experimental accuracy of the line positions in our measurements.

The second term in Eq. (1), the indirect coupling of the electronic spin and the molecular rotation, which leads to fine structure, can be written as an effective Hamiltonian [26,27]

$$H_{\mathrm{SR}} = \frac{1}{2}\sum_{ij}\varepsilon_{ij}\left(N_i S_j + S_j N_i\right). \tag{3}$$

For an asymmetric top this gives a spin–rotation energy

$$E_{\mathrm{SR}} = \tfrac{1}{2}\varepsilon_N[J(J+1) - N(N+1) - S(S+1)], \tag{4}$$

where, for a molecule with C_{2v} symmetry, ε_N can be written in terms of diagonal tensor elements only

$$\varepsilon_N = \frac{1}{2}(\varepsilon_{bb}+\varepsilon_{cc}) + \frac{\varepsilon_{aa} - \frac{1}{2}(\varepsilon_{bb}+\varepsilon_{cc})}{N(N+1)}K^2 \pm \frac{1}{4}\delta_{|K|,1}(\varepsilon_{bb}-\varepsilon_{cc}). \tag{5}$$

The + and − sign corresponds to the symmetric and antisymmetric Wang combination of symmetric top functions, respectively, and $\delta_{|K|,1}$ is unequal to zero for $|K| = 1$. Eq. (5) is identical to Eq. (6) of [26] if x, y, and z are substituted by c, b, and a, respectively. The off-diagonal contributions $(H_{\mathrm{SR}})_{N-1,N}$ and $(H_{\mathrm{SR}})_{N,N+1}$ are often small enough to be disregarded here [28,29]. According to Eq. (3) each rotational level is split into two levels, with $J = N + \frac{1}{2}$ and $J = N - \frac{1}{2}$, leading to respective energy shifts of $\frac{1}{2}N\varepsilon_N$ and $-\frac{1}{2}(N+1)\varepsilon_N$. For the electronic and vibrational ground state, the fine structure coupling is relatively small. In the fit program we have used the values determined in [30]: $\varepsilon''_{aa} = 0.180\ cm^{-1}$, $\varepsilon''_{bb} = 0.000\ cm^{-1}$, and $\varepsilon''_{cc} = -0.003\ cm^{-1}$. For the $K = 0$ stacks only $\bar{\varepsilon} = (\varepsilon_{bb} + \varepsilon_{cc})/2$ matters and for the ground state this value can be neglected.

From the fitted ε' values listed in the overview tables (Tables 3 and 4) it becomes clear that both magnitude and sign vary greatly between different vibronic states. This variety is the very consequence of vibronic interactions, since the ε' values depend strongly on the degree of mixing of the coupled states. As a consequence, the $\bar{\varepsilon}'$ value that according to Eq. (5) affects the line positions of both the $K = 0$ and $K = 1$ stack, not necessarily has to be treated as a common parameter for both stacks. Therefore it is also possible to use two independent fit parameters: $\bar{\varepsilon}'_{K=0}$ and $\bar{\varepsilon}'_{K=1}$. This seems to be inconsistent with the assumption that the effective rotational constant, $\bar{B}' \equiv \frac{1}{2}(B' + C')$, should be equal for both stacks, but in practice this assumption turns out to be a good approximation. Indeed, $\bar{B}'$ values turn out to be much less sensitive to (ro)vibronic coupling than $\bar{\varepsilon}'$ values. We have applied this

procedure—besides the standard procedure used for all bands—only in the case of the strong 14851 cm^{-1} band (Section 3.5).

The last term in Eq. (1), the centrifugal distortion, is written as

$$H_{cf} = D_N N^2 (N+1)^2. \quad (6)$$

On the basis of experimental data [31], D_N is expected to be of the order of 10^{-4} cm^{-1} and its contribution for the lowest N values—as typically observed in a molecular beam experiment—is negligible. An exception is the 14851 cm^{-1} band and in this particular case inclusion of D'_N improves the fit.

Finally, the relative line intensities, as determined by rotational temperature, are also calculated. In the fitting procedure, however, this information is only used to guide the assignment. Particularly for larger frequency domains deviations between observed and calculated intensities may occur, because of experimental features, such as saturation, dye gain profile, and wavelength dependent sensitivity of the detector. Since we only fit line positions and not intensities, the model is approximately linear in the spectral parameters that we use. Assuming that the experimental errors are normally distributed, the standard errors of the fit are taken as the square roots of the diagonal elements of the covariance matrix. The covariances are found to be very small.

Below, in Sections 3.1–3.4, vibronic bands corresponding to four different spectral classes are discussed and illustrated with typical examples that have been fit to the equations listed in the previous paragraphs. It is important to note that we label the bands according to their experimental appearance: i.e., laser bandwidth and sensitivity determine, respectively, whether fine structure is resolved or not and weaker (particularly $K = 1$) transitions are detected or not. The classification only reflects the spectroscopic level at which a vibronic band can be described.

The majority of the fits yields acceptable values for the rotational constants—apart from bands that are heavily perturbed—and in the few cases where this is not the case, it is indicated that the resulting molecular constants should be used as effective parameters only. In general the error $\Delta(\frac{1}{2}(B' + C'))$ is a good measure for the accuracy of the fit. A comparison of the constants is important to conclude about the degree of mixing of the two lowest electronic states. In addition, all vibrational bands can be analyzed in terms of density statistical distribution and a comparison with previous results for the main isotopologue is made. These topics are addressed in Section 4.

3.1. K = 0 stack only, with unresolved spin splittings

In Fig. 2 one of nearly 80 vibronic bands is shown for which only $K = 0$ transitions have been observed. Only rotational transitions starting from even N-levels are symmetry allowed and as a consequence the spectrum consists of two branches with $P_{2,4,6}$ and $R_{0,2,4,6}$ transitions, separated by a band gap of $6[(B'' + C'')/2] \equiv 6\overline{B}''$. Q-branch transitions are not allowed in the $K = 0$ stack. The assignment is indicated in the figure. Note that a $K = 1$ stack should exist in the vicinity of each $K = 0$ stack. However, the $K = 1$ stack is always significantly weaker than the $K = 0$ stack, particularly because of rotational cooling in the expansion; the rotational state summed intensity of the $K = 1$ stack is expected to be about half that of the $K = 0$ stack at a rotational temperature of 8 K. In addition, the number of transitions in the $K = 1$ stack is larger than for the $K = 0$ stack (see Section 3.2) and these transitions are more likely involved in rovibronic couplings because of the increased number of coupling pathways. As a consequence, the intensity may be dispersed over a significantly larger number of lines and $K = 1$ stack transitions may not be observable. The "grass" of weak lines observable in Fig. 2, for example, is expected to be due, at least partially, to the corresponding $K = 1$ stack. It is also possible that a $K = 1$ band shifts outside its corresponding $K = 0$ band, which makes an identification very hard. Without a $K = 1$ band it is not possible to determine independent values for B' and C'. For the band shown in Fig. 2 a fit routine following Eq. (2) results in $\nu_{bo} = 15\,420.5(1)$ cm^{-1} and $\overline{B}' = 0.426(5)$ cm^{-1}. The deviations between observed and calculated line positions are well within the experimental uncertainty of a few hundredths of a cm^{-1}. In Table 3 an overview of all 'only' $K = 0$ bands is given and these are labeled with an A. Note that for $K = 0$ the asymmetric top contributions in Eq. (2)—C_1, C_2, and C_3—are zero.

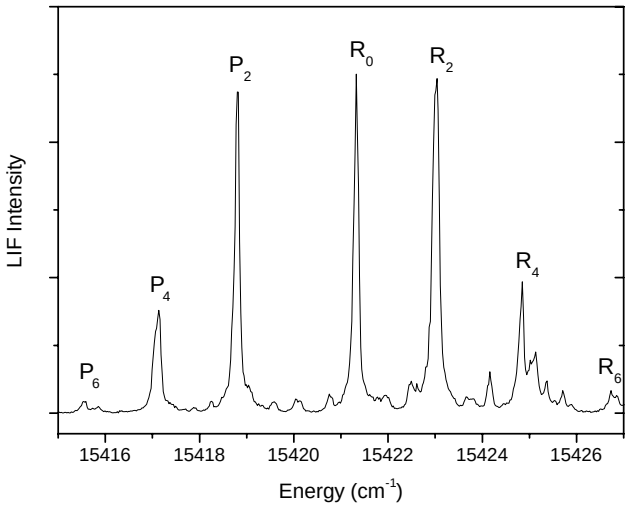

Fig. 2. An example of an 'only' $K = 0$ stack within the A^2B_2–X^2A_1 electronic system of $^{15}NO_2$ observed around 15 420.5 cm^{-1} without observable spin splitting. The band is listed as No. 55 in Table 3.

3.2. K = 0 and K = 1 stacks with unresolved spin splittings

Roughly 50 vibronic bands show recognizable $K = 1$ transitions in addition to $K = 0$ transitions. An example is shown in Fig. 3. Apart from the $K = 0$ $P_{2,4,6,8}$ and

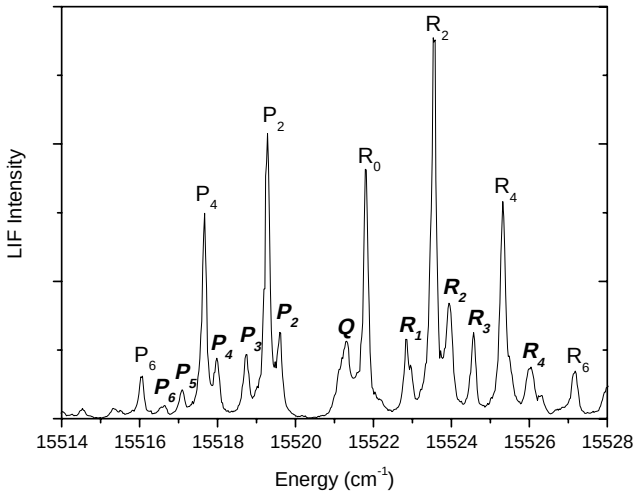

Fig. 3. An example of an electronic A^2B_2–X^2A_1 transition of $^{15}NO_2$ consisting of both $K = 0$ and $K = 1$ stacks. Fine structure is not resolved. Note the difference in symmetry allowed transitions for the $K = 0$ (only even) and $K = 1$ (both odd and even levels). The band is centered around 15521 cm^{-1} and listed in Tables 3 and 4 as No. 60.

$R_{0,2,4,6}$ progressions also the $K = 1$ P_{2-6} and R_{1-4} transitions as well as a Q-branch are identified. For the $K = 1$ band, transitions starting both from even and odd N-levels are observed.

All line positions (summarized in Table 1) are fitted simultaneously, using Eq. (2), which results in independent values for A', B', and C'. For the band shown in Fig. 3 values $\nu_{bo} = 15520.9(1)\ cm^{-1}$, $A' = 7.952(5)\ cm^{-1}$, $B' = 0.458(5)\ cm^{-1}$, and $C' = 0.398(5)\ cm^{-1}$ have been found. An unambiguous combined $K = 0$ and $K = 1$ analysis is possible only in about 20 of the 50 observed bands. This is due to a combination of factors as explained above. In addition, several $K = 1$ bands are irregular and because of the limited number of rotational transitions at the low temperature in the expansion, assignments are not always possible. In Table 3 an overview of all assigned $K = 0$ sub-bands is given. These bands are labeled with B and the corresponding $K = 1$ parameters—as far as assigned—are listed in Table 4.

Table 1
Observed and calculated line positions for both $K = 0$ and $K = 1$ stacks of the band at 15520.9(1) cm^{-1} in the A^2B_2–X^2A_1 electronic system of $^{15}NO_2$ as shown in Fig. 3

	ν_{obs}	ν_{calc}	Obs. − calc.
$K = 0$			
P_6	15516.02	15516.07	−0.05
P_4	15517.66	15517.65	0.02
P_2	15519.28	15519.27	0.01
R_0	15521.80	15521.80	0.00
R_2	15523.58	15523.55	0.02
R_4	15525.32	15525.34	−0.02
R_6	15527.17	15527.16	0.01
$K = 1$			
P_6	15516.61	15516.57	0.04
P_5	15517.09	15517.05	0.04
P_4	15517.98	15518.02	−0.04
P_3	15518.73	15518.75	−0.02
P_2	15519.61	15519.58	0.03
Q_1	15521.31	15521.33	−0.02
R_1	15522.90	15522.93	−0.03
R_2	15523.94	15524.01	−0.07
R_3	15524.57	15524.53	0.04
R_4	15526.02	15525.98	0.04
R_5	15526.24	15526.25	−0.02

All values are in cm^{-1}.

3.3. $K = 0$ & $K = 0$ and $K = 1$ transitions with observed spin splittings

An example of a $K = 0$ band with spin splitting is presented in Fig. 4. The band comprises $P_{2,4,6}$ and $R_{0,2,4,6}$ transitions and for each rovibronic transition a spin splitting is resolved. The two spin components correspond to

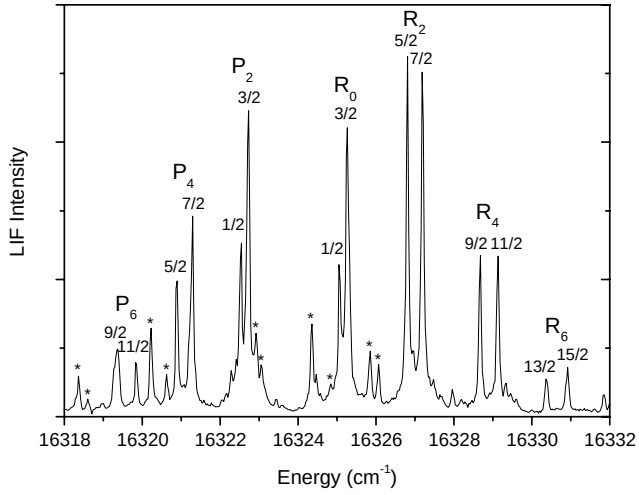

Fig. 4. An example of a $K = 0$ sub-band with resolved fine structure splitting in the electronic A^2B_2–X^2A_1 transition of $^{15}NO_2$, centered around 16324.3 cm^{-1}. The fine structure components are indicated in the figure. Transitions marked with an asterisk have been identified as the $K = 1$ stack of this band. In Tables 3 and 4 this band is listed under No. 108.

Table 2
Observed and calculated line positions for the $K = 0$ transition of the band at 16324.3(1) cm^{-1} in the A^2B_2–X^2A_1 system of $^{15}NO_2$ with resolved fine structure (Fig. 4)

$K = 0$		ν_{obs}	ν_{calc}	Obs. − calc.
P_6	(9/2)	16319.37	16319.36	0.01
P_6	(11/2)	16319.85	16319.89	−0.03
P_4	(5/2)	16320.89	16320.91	−0.02
P_4	(7/2)	16321.29	16321.25	0.04
P_2	(1/2)	16322.54	16322.57	−0.03
P_2	(3/2)	16322.72	16322.71	0.01
R_0	(1/2)	16325.07	16325.10	−0.03
R_0	(3/2)	16325.27	16325.24	0.02
R_2	(5/2)	16326.81	16326.82	−0.01
R_2	(7/2)	16327.19	16327.15	0.05
R_4	(9/2)	16328.67	16328.63	0.04
R_4	(11/2)	16329.13	16329.16	−0.03

All values are in cm^{-1}.

states in which spin and rotational angular momentum are parallel ($J' = N' + \frac{1}{2}$) or anti-parallel ($J' = N' - \frac{1}{2}$). The sign of $\overline{\varepsilon}'$ is determined by the intensity pattern of the lowest fine structure components in the spectrum. The corresponding labeling is indicated in the figure. In this particular example the spin splitting increases linearly with N in the $K = 0$ stack. The line positions are summarized in Table 2. The frequencies are fitted following Eqs. (2) and (4), which gives $\nu_{bo} = 16324.3(1)\ cm^{-1}$, $\overline{B}' = 0.434(5)\ cm^{-1}$, and $\overline{\varepsilon}' = 0.094\ cm^{-1}$. In Table 3 the molecular parameters are listed of $K = 0$ bands with fine structure. These bands are labeled C.

3.4. Perturbed and irregular transitions

About 40 bands (labeled D in Table 3) were found to be rotationally perturbed. The majority of these bands are so irregular that in view of the limited number of transitions rotational assignments are not possible. For these bands only approximate values for the band origins are listed in Table 3.

In some cases, however, the rovibronic interaction is limited to a single rovibronic level. In Fig. 5 a spectrum is shown in which a $K = 0$ sub-band with a resolved spin splitting displays the same triplet of lines for both the R_2 and the P_4 transition. This means that one of the two spin components of the $N = 3$ level is split into two components because of an interaction with a dark level. In this particular case the spin component $J = 7/2$ of the $N = 3$ excited rotational state interacts. For the fit, the deperturbed energy of the $J = 7/2$ level is used yielding $\nu_{bo} = 16173.5(1)\ cm^{-1}$, $\overline{B}' = 0.441(5)\ cm^{-1}$, and $\overline{\varepsilon}' = -0.090\ cm^{-1}$.

An overview of all observed bands is given in Table 3. The labeling indicates the type of the transition: A_0, $B_{0,1}$, C_0 and $C_{0,1}$, and D refer to the corresponding previous subsections and the subscript indicates the observed K values. Bands that have not been fitted are only represented by an (estimated) band origin. The fitted $K = 1$ bands are listed separately in Table 4. Most of the $\frac{1}{2}(B' + C')$ values derived for corresponding $K = 0$ and $K = 1$ stacks agree to within $0.001\ cm^{-1}$.

All observed bands have been numbered, except for two types of band: for non-assignable bands of type D only band origins have been extracted and for bands above $17260\ cm^{-1}$ it is not possible to discriminate hot bands starting from (0,1,0) as the corresponding cold bands are above $18000\ cm^{-1}$ and have not been recorded.

From these overview tables with band origins and excited state parameters it is straightforward to identify hot bands and spurious bands belonging to $^{14}NO_2$. Hot bands are indicated by HB and the number of the corresponding cold band. The final result is that in total 177 cold bands—each of them corresponding to a vibronic level with $^2B_2$ symmetry—have been identified between 14300 and $17260\ cm^{-1}$ (see Tables 3 and 4).

3.5. The 14851 cm^{-1} band: a benchmark transition for remote sensing

In polyad 7 we have located an exceptionally strong cold band transition that is centered around $14851\ cm^{-1}$. The band is indicated by an asterisk in Fig. 1 and has the spectral features typical for a band as discussed in Section 3.3. At this stage it is unclear why this band is so intense. Also the corresponding hot band transition—located in a fast scan around $14110\ cm^{-1}$—is very intense and dominates the spectral region of polyad 6. As there is barely any overlap between the $14851\ cm^{-1}$ band with known $^{14}NO_2$ bands, we pay special attention to this band because of its potential use for atmospheric remote $^{15}NO_2$ sensing. Last year data obtained from satellite observations by GOME and SCIAMACHY [32,33] showed the existence of very high NO_2 column densities, particularly above industrialized areas. An additional tool in understanding the complex system of atmospheric processes leading to NO_x production is the study of isotope distributions in the atmosphere. For ozone (and several other atmospheric gases) an anomalous distribution has been found that has been attributed to the isotope shift of the zero-point energies [34–36]. Similar observations are expected for NO_2 isotopologues, but good benchmark transitions for remote sensing have been missing so far. The $14851\ cm^{-1}$ band presented here is a good candidate to overcome this problem.

A detailed view of this band with a rotational assignment is shown in Fig. 6. Both for the $K = 0$, and for the $K = 1$ stack, transitions up to $N = 8$ have been observed. This makes it possible to fit the maximum number of 9 spectroscopic parameters that are taken into account: the band origin, A', B', C', $\overline{\varepsilon}'(K = 0)$, ε'_{aa}, ε'_{bb}, ε'_{cc} ($K = 1$) and the centrifugal distortion constant D'_N. By varying the experimental conditions, spectra have been taken at different rotational temperatures, which unfortunately span only a short range. Comparison of the fit results for two spectra at estimated rotational temperatures of 7 and 9 K shows that the calculated parameters for the two cases are equal within the estimated errors at the 95% confidence level. The deviations between the two origins, $14851.24\ cm^{-1}$ for $T_{rot} = 9$ K, versus $14851.31\ cm^{-1}$ for $T_{rot} = 7$ K, reflects the uncertainty in absolute frequency calibration. The 9 K spectrum is displayed in Fig. 6, together with the fitted spectrum. The calculated $K = 0$ and $K = 1$ stack spectra are shown on top, to make clear how the subspectra are superimposed.

The assigned experimental line positions are compared with the calculated ones in Table 5. The resulting fit parameters are given in Table 6. Even for this favorable case, where the fit is based on many line positions, the ε' parameters for the $K = 1$ stack have large uncertainties, and therefore are least suited for comparison of different vibronic bands. In contrast, the fine structure parameter, $\overline{\varepsilon}'$ of the $K = 0$ stack, can be determined with great accuracy. Also the centrifugal distortion constant, D'_N, is very important for obtaining a good fit, even if it is very small.

Table 3
Overview of all rovibronic bands observed in the A^2B_2–X^2A_1 electronic system of $^{15}NO_2$ in the 14300–18000 cm^{-1} region

	Origin	Origin cold band	Intensity (a.u.)	$\frac{1}{2}(B'+C')$	$\frac{1}{2}(\varepsilon'_{bb}+\varepsilon'_{cc})$	$\Delta(\frac{1}{2}(B'+C'))$ (10^{-3})	X^2A_1 level	Type
1	14283.91		3.4	0.421	0	1.4		A_0
2	14292.26		5.9	0.428	−0.057	0.9		C_0
HB37	14317.97	15057.93	3.6	0.403	0	1.4	(0,1,0)	A_0
3	14341.16		2.8	0.444	0	0.6		A_0
HB39	14361.91	15101.93	10.1	0.439	0.086	0.6	(0,1,0)	D
HB40	14373.79	15113.81	5.8	0.445	−0.066	1.4	(0,1,0)	C_0
4	14387.76		2.7	0.388	−0.058	1.6		$C_{0,1}$
5	14416.08		57.0	0.382	−0.327	1.4		C_0
6	14418.19		3.5	0.447	0	1.4		A_0
	14423.00							D
HB42	14450.88	15190.91	10.3	0.428	0	1.4	(0,1,0)	A_0
HB43	14456.48	15196.45	3.0	0.405	0	1.4	(0,1,0)	A_0
7	14479.61		1.6	0.413	0	0.6		A_0
8	14497.49		5.7	0.391	−0.134	1.4		C_0
9	14510.99		0.6	0.401	0	1.7		A_0
HB45	14530.58	15270.60	10.4	0.421	0.028	0.6	(0,1,0)	C_0
HB46	14545.79	15285.74	12.7	0.437	−0.020	0.6	(0,1,0)	C_0
10	14562.56		1.7	0.437	0.108	1.7		C_0
11	14577.28		7.1	0.416	0.020	1.0		C_0
HB47	14581.08	15320.98	9.0	0.381	0.331	1.4	(0,1,0)	C_0
HB48	14591.68	15331.65	2.3	0.416	0.030	1.4	(0,1,0)	C_0
HB49	14599.52	15339.47	9.7	0.418	−0.025	0.7	(0,1,0)	C_0
12	14615.16		8.2	0.424	−0.027	0.5		C_0
13	14645.56		15.6	0.415	−0.014	0.4		C_0
HB50	14650.49	15390.45	1.6	0.414	0	1.4	(0,1,0)	A_0
14	14660.71		7.5	0.410	0.098	1.6		C_0
HB51	14663.31	15403.22	7.5	0.424	0	0.6	(0,1,0)	A_0
15	14675.20		88.2	0.419	−0.109	1.4		$C_{0,1}$
16	14694.83		2.5	0.450	0.066	0.6		C_0
17	14710.33		25.4	0.417	−0.109	0.6		C_0
18	14739.74		26.6	0.425	0.036	0.6		C_0
HB58	14749.47	15489.38	9.0	0.434	0.086	0.6	(0,1,0)	C_0
19	14765.09		24.9	0.442	0.040	0.5		C_0
HB60	14781.00	15520.96	83.6	0.427	0	0.3	(0,1,0)	$B_{0,1}$
20	14791.78		9.9	0.426	−0.049	0.7		C_0
HB61	14800.74	15540.58	5.2	0.431	−0.052	1.8	(0,1,0)	C_0
HB62	14819.02	15559.09	45.5	0.435	0.056	0.9	(0,1,0)	C_0
HB63	14825.40	15565.47	20.5	0.433	0	1.4	(0,1,0)	D
21	14840.77		16.9	0.421	0	0.6		A_0
22	14851.27		360.0	0.463	0.105	0.3		$C_{0,1}$
23	14892.48		2.7	0.405	0.070	0.7		C_0
24	14900.63		10.7	0.409	0.044	0.7		C_0
HB68	14907.59	15647.90	44.7	0.458	0	1.4	(0,1,0)	A_0
HB69	14916.79	15656.78	15.4	0.426	−0.065	0.6	(0,1,0)	C_0
25	14931.66		2.7	0.403	−0.061	1.4		C_0
26	14934.25		4.3	0.425	0.041	1.7		C_0
HB104	14940.99	16247.61	8.3	0.444	−0.014	0.9	(1,0,0)	C_0
27	14941.70		5.0	0.420	−0.033	0.9		C_0
28	14960.50		8.2	0.441	−0.044	1.8		C_0
29	14962.75		10.2	0.403	0	0.6		A_0
30	14973.93		5.0	0.417	−0.039	0.6		C_0
31	14987.49		7.5	0.434	−0.548	1.4		C_0

The bands are numbered and the label 'HB' links a hot band to the corresponding cold band transition. The 'type' refers to the labeling used in the text to classify the spectral appearance of a band. The subscript indicates a $K=0$ or $K=1$ band. The molecular parameters of $K=1$ bands are listed separately in Table 4. The intensity is given in arbitrary units and all other values are given in cm^{-1}. $\Delta(\frac{1}{2}(B'+C'))$ $(10^{-3}\ cm^{-1})$ gives an uncertainty of one standard deviation and is a measure for the quality of the fit.

[a] These values are unrealistic small and should be considered as effective constants only.

Table 3 (*continued*)

	Origin	Origin cold band	Intensity (a.u.)	$\frac{1}{2}(B'+C')$	$\frac{1}{2}(\varepsilon'_{bb}+\varepsilon'_{cc})$	$\Delta(\frac{1}{2}(B'+C'))$ (10^{-3})	X^2A_1 level	Type
	14990.00							*D*
HB75	14992.15	15732.12	13.2	0.412	0	0.3	(0,1,0)	A_0
32	14997.94		4.1	0.426	0	0.6		A_0
33	15010.05		2.0	0.389	0.210	1.4		*D*
34	15017.83		2.3	0.438	0.105	1.6		C_0
35	15023.94		9.2	0.403	−0.057	0.6		$C_{0,1}$
36	15038.58		1.7	0.474	0	1.4		A_0
	15040.00							*D*
HB78	15048.00	15787.91	3.8	0.414	0	0.6	(0,1,0)	A_0
37	15057.93		20.7	0.409	−0.049	0.6		$C_{0,1}$
HB80	15069.05	15808.95	2.2	0.398	0	0.6	(0,1,0)	A_0
38	15090.66		1.2	0.398	0	0.6		A_0
	15101.00							*D*
39	15101.93		41.9	0.404	0.109	2.0		*D*
40	15113.81		23.6	0.430	−0.062	0.6		C_0
HB82	15130.68	15870.65	1.8	0.417	0.044	0.6	(0,1,0)	C_0
41	15147.25		0.7	0.402	0	1.7		A_0
HB84	15167.99	15908.02	6.9	0.428	−0.028	0.5	(0,1,0)	C_0
HB85	15179.27	15919.20	18.7	0.398	0.029	0.6	(0,1,0)	C_0
42	15190.91		79.8	0.420	0	0.5		*D*
43	15196.45		15.2	0.409	0	0.6		A_0
HB86	15204.48	15944.35	13.2	0.385	−0.112	0.9	(0,1,0)	C_0
HB87	15211.99	15951.92	26.4	0.441	0.009	0.3	(0,1,0)	*D*
44	15225.23		4.8	0.415	−0.088	0.6		C_0
HB88	15239.74	15979.68	2.2	0.406	−0.029	0.6	(0,1,0)	C_0
45	15270.60		30.4	0.421	0.027	0.3		C_0
46	15285.74		96.7	0.437	0	0.5		A_0
47	15287.88		72.1	0.438	0.106	1.4		C_0
48	15302.51		6.8	0.430	0.096	0.6		*D*
49	15320.98		83.9	0.377	0.276	0.5		C_0
50	15331.65		8.8	0.406	0	0.6		A_0
51	15339.47		51.9	0.421	−0.024	0.3		C_0
HB96	15352.38	16092.36	14.9	0.407	0.009	0.9	(0,1,0)	C_0
HB148	15382.81	16861.75	2.6	0.437	0.099	1.4	(0,2,0)	C_0
52	15390.45		7.3	0.411	0	0.6		A_0
53	15403.22		103.6	0.422	0	0.3		A_0
54	15404.89		73.7	0.439	0	1.4		A_0
55	15420.47		45.0	0.426	0	0.5		A_0
	15433.00							*D*
	15434.89		14.9	0.453	0.069	0.7		$^{14}NO_2$
56	15449.81		25.0	0.447	−0.215	1.4		C_0
HB101	15461.99	16201.94	4.0	0.391	−0.059	0.9	(0,1,0)	C_0
HB102	15468.47	16208.51	2.7	0.420	−0.131	1.0	(0,1,0)	C_0
	15476.87		1.0	0.413	0	1.4		$^{14}NO_2$
57	15485.69		42.8	0.418	0.095	0.9		C_0
58	15489.38		64.3	0.434	0.084	0.3		C_0
	15501.00							*D*
HB104	15507.61	16247.61	18.2	0.441	0	0.6	(0,1,0)	A_0
59	15508.90		20.4	0.394	0	0.6		A_0
60	15520.95		115.5	0.427	0	0.2		$B_{0,1}$
	15533.00							*D*
61	15540.58		19.1	0.456	0	1.4		A_0
62	15559.09		96.6	0.432	0.058	0.6		C_0
63	15565.47		75.7	0.417	0.060	0.6		C_0
64	15576.67		21.0	0.413	0	0.5		A_0
HB108	15584.38	16324.32	45.7	0.435	0.102	0.6	(0,1,0)	C_0
65	15587.17		34.1	0.418	−0.085	0.6		C_0

Table 3 (*continued*)

	Origin	Origin cold band	Intensity (a.u.)	$\frac{1}{2}(B'+C')$	$\frac{1}{2}(\varepsilon'_{bb}+\varepsilon'_{cc})$	$\Delta(\frac{1}{2}(B'+C'))$ (10^{-3})	X^2A_1 level	Type
	15603.00							*D*
66	15607.22		1.1	0.432	0	0.6		A_0
	15614.79		1.7	0.440	0	0.6		$^{14}NO_2$
67	15622.92		0.7	0.415	0	0.6		A_0
68	15647.90		84.1	0.433	0	0.4		$C_{0,1}$
69	15656.78		56.2	0.426	−0.063	0.3		C_0
70	15663.12		33.0	0.416	−0.039	0.3		C_0
71	15675.88		2.4	0.410	0	0.6		A_0
HB113	15676.21	16416.10	1.8	0.411	0.054	1.6	(0,1,0)	C_0
HB113	15683.80	16423.76	0.5	0.414	0	1.1	(0,1,0)	C_0
HB115	15695.65	16435.58	27.4	0.435	0.093	0.7	(0,1,0)	C_0
72	15701.07		26.6	0.380	−0.114	0.6		C_0
HB116	15706.70	16446.57	4.1	0.388	0	1.7	(0,1,0)	A_0
73	15712.94		1.7	0.423	0	0.6		A_0
HB117	15713.87	16453.74	7.1	0.399	0	0.5	(0,1,0)	A_0
74	15722.78		1.7	0.414	0.179	0.6		C_0
75	15732.12		65.7	0.411	0	0.3		$C_{0,1}$
HB118	15736.94	16476.96	31.1	0.423	0	0.6	(0,1,0)	A_0
76	15749.80		1.8	0.432	0	1.4		A_0
HB119	15767.65	16507.61	2.8	0.416	0	1.4	(0,1,0)	A_0
HB121	15772.67	16512.67	10.2	0.419	0.026	1.6	(0,1,0)	C_0
77	15778.52		15.6	0.473	0	1.4		A_0
78	15787.91		29.1	0.415	0	0.3		A_0
79	15793.09		15.0	0.422	0	0.6		A_0
80	15808.95		14.9	0.400	0.008	0.3		C_0
81	15819.11		9.3	0.393	0.060	0.5		C_0
	15842.00							*D*
HB128	15861.14	16601.05	6.0	0.418	−0.194	0.9	(0,1,0)	*D*
82	15870.65		5.3	0.416	0.050	0.6		C_0
HB130	15884.02	16623.92	4.4	0.414	0.161	0.6	(0,1,0)	C_0
83	15892.51		1.0	0.417	0	1.4		A_0
HB131	15895.59	16635.55	3.0	0.424	−0.037	0.9	(0,1,0)	C_0
84	15908.02		22.9	0.422	−0.022	0.3		C_0
85	15919.20		47.8	0.397	0.029	0.6		$C_{0,1}$
HB135	15931.68	16671.63	12.6	0.401	0	0.3	(0,1,0)	A_0
HB136	15943.44	16683.46	37.7	0.415	0	0.5	(0,1,0)	A_0
86	15944.35		35.5	0.396	−0.124	0.6		C_0
87	15951.92		73.4	0.444	0.029	0.6		C_0
HB137	15962.38	16702.33	14.8	0.392	−0.101	1.4	(0,1,0)	C_0
HB138	15970.11	16710.12	34.3	0.377	−0.163	1.4	(0,1,0)	$C_{0,1}$
88	15979.68		5.0	0.406	−0.027	0.6		C_0
89	15987.80		5.6	0.409	0.099	0.6		C_0
90	15992.73		1.4	0.412	0	1.4		A_0
91	16000.95		5.0	0.467	−0.523	1.4		C_0
92	16014.81		6.8	0.382	0.086	1.4		C_0
93	16023.90		98.8	0.410	−0.025	0.3		C_0
HB141	16036.68	16776.59	3.5	0.406	0.093	1.6	(0,1,0)	C_0
HB142	16040.26	16780.32	12.6	0.406	0.045	1.4	(0,1,0)	C_0
94	16044.86		9.7	0.394	0	0.3		A_0
95	16059.71		53.8	0.432	−0.176	1.4		C_0
HB145	16081.00	16821.05	2.8	0.423	0.062	1.4	(0,1,0)	C_0
96	16092.36		46.8	0.405	0.009	0.5		C_0
	16095.00							*D*
HB148	16121.71	16861.75	14.1	0.443	0.075	0.5	(0,1,0)	$C_{0,1}$
97	16138.29		6.8	0.401	0	1.4		A_0
98	16145.01		124.1	0.418	0.079	0.3		$C_{0,1}$
HB152	16159.90	16899.86	5.2	0.402	−0.045	0.6	(0,1,0)	C_0
99	16173.48		43.9	0.441	−0.090	0.5		*D*
100	16181.06		5.9	0.401	0	0.6		A_0
HB	16195.40	17500.36	5.4	0.400	−0.022	0.6	(1,0,0)	C_0

(*continued on next page*)

Table 3 (*continued*)

	Origin	Origin cold band	Intensity (a.u.)	$\frac{1}{2}(B'+C')$	$\frac{1}{2}(\varepsilon'_{bb}+\varepsilon'_{cc})$	$\Delta(\frac{1}{2}(B'+C'))$ (10^{-3})	X^2A_1 level	Type
101	16201.94		23.0	0.392	−0.059	0.9		C_0
102	16208.51		11.2	0.380	−0.099	0.6		C_0
	16225.00							D
103	16241.55		26.0	0.475	0.069	1.4		C_0
104	16247.61		119.3	0.436	0.039	0.3		C_0
105	16251.40		26.2	0.423	0.039	0.6		C_0
106	16267.12		73.4	0.426	0	0.2		$C_{0,1}$
	16284.00							D
107	16297.51		79.3	0.415	−0.043	0.3		C_0
108	16324.32		124.0	0.434	0.094	0.5		$C_{0,1}$
109	16343.22		7.8	0.423	−0.112	0.6		C_0
110	16361.60		5.3	0.434	−0.438	1.4		D
	16373.00							D
111	16382.05		5.3	0.417	−0.081	0.5		C_0
	16393.00							D
112	16407.37		6.2	0.410	0.100	0.6		C_0
113	16416.10		18.1	0.415	0.063	0.5		$C_{0,1}$
114	16423.76		5.0	0.414	0	1.4		A_0
115	16435.58		92.2	0.436	0.101	0.4		$C_{0,1}$
116	16446.57		25.6	0.395	−0.037	0.6		C_0
117	16453.74		28.5	0.403	−0.016	0.3		C_0
118	16476.96		41.1	0.421	0	0.3		A_0
119	16480.41		32.4	0.405	−0.090	0.6		C_0
	16490.00							D
120	16507.61		16.3	0.416	0	0.2		A_0
121	16512.67		40.7	0.417	0.029	0.5		$C_{0,1}$
122	16528.84		4.0	0.345[a]	0	1.4		D
123	16529.65		4.9	0.470	0	1.4		D
124	16545.72		1.7	0.419	−0.057	1.7		C_0
125	16550.83		12.2	0.389	−0.164	1.4		C_0
126	16554.64		13.9	0.422	0.049	0.6		C_0
127	16578.51		68.2	0.415	0.273	0.5		C_0
	16580.00							D
	16582.00							D
128	16601.05		41.6	0.433	−0.143	0.5		C_0
129	16616.15		8.7	0.437	0.199	0.9		C_0
130	16623.92		29.6	0.418	0.110	0.5		C_0
131	16635.55		12.8	0.418	−0.040	0.6		C_0
132	16638.40		11.0	0.421	0.043	1.5		C_0
133	16641.59		11.5	0.322[a]	0.040	1.4		C_0
134	16656.98		0.7	0.428	0.157	1.4		C_0
135	16671.63		57.4	0.401	0	0.3		$B_{0,1}$
136	16683.46		109.4	0.417	−0.052	0.3		C_0
137	16702.33		94.9	0.391	−0.101	0.5		C_0
138	16710.12		160.5	0.361[a]	−0.138	0.5		C_0
139	16712.27		31.4	0.400	0	0.7		A_0
	16728.00							D
HB	16760.32	17500.36	14.1	0.416	−0.020	1.0	(0,1,0)	C_0
140	16763.92		22.0	0.399	0.035	0.6		C_0
141	16776.59		58.2	0.448	0.101	0.6		C_0
142	16780.32		50.8	0.395	0.082	0.6		C_0
143	16796.72		51.9	0.435	−0.036	1.4		C_0
	16800.00							D
144	16803.18		172.7	0.451	0.218	1.4		C_0
	16808.00							D
145	16821.05		46.7	0.419	0.054	0.3		C_0
146	16836.07		61.5	0.411	0	0.3		C_0
147	16851.41		10.8	0.380	0.020	0.6		C_0
148	16861.75		253.0	0.432	0.052	0.3		$C_{0,1}$

Table 3 (*continued*)

	Origin	Origin cold band	Intensity (a.u.)	$\frac{1}{2}(B'+C')$	$\frac{1}{2}(\varepsilon'_{bb}+\varepsilon'_{cc})$	$\Delta(\frac{1}{2}(B'+C'))$ (10^{-3})	X^2A_1 level	Type
149	16873.69		67.2	0.465	0.184	1.4		*D*
150	16886.97		160.2	0.409	−0.088	0.5		C_0
151	16889.24		159.4	0.413	0.054	0.6		C_0
152	16899.86		72.5	0.401	−0.041	0.5		C_0
153	16913.67		173.4	0.411	0.210	0.5		$C_{0,1}$
154	16919.94		54.6	0.391	−0.030	1.0		C_0
155	16932.23		48.4	0.407	0	0.5		A_0
	16933.00							*D*
156	16941.95		36.8	0.413	0.059	0.6		*D*
157	16954.30		30.7	0.453	0.093	0.6		C_0
158	16955.52		43.8	0.464	−0.015	1.6		C_0
159	16968.43		38.7	0.403	−0.109	0.5		C_0
160	16973.16		33.4	0.410	0	0.5		A_0
161	17004.10		349.8	0.394	0.165	0.8		C_0
162	17018.69		145.8	0.467	0.194	0.8		C_0
163	17029.36		176.2	0.405	0.215	1.4		*D*
164	17046.61		2.3	0.425	0	0.6		A_0
165	17071.06		59.8	0.386	−0.070	0.3		C_0
166	17076.93		31.1	0.390	0.048	0.5		C_0
	17092.07		16.7	0.414	0	0.5		$^{14}NO_2$
167	17097.53		22.5	0.410	−0.106	0.6		C_0
168	17111.44		31.6	0.310[a]	−0.146	1.4		*D*
169	17113.28		24.8	0.466	0.150	0.7		*D*
170	17126.02		1.5	0.405	0.022	1.7		C_0
HB	17146.90	17886.86	14.3	0.421	0.079	0.6	(0,1,0)	C_0
171	17158.15		6.9	0.398	0.026	1.4		C_0
172	17169.76		100.2	0.370	−0.032	0.5		$C_{0,1}$
HB	17180.95	17920.88	2.5	0.413	0	1.7	(0,1,0)	C_0
HB	17192.67	17932.57	1.6	0.430	0	1.7	(0,1,0)	C_0
173	17202.12		7.9	0.404	−0.077	1.6		C_0
174	17208.29		30.6	0.395	−0.158	1.4		C_0
175	17218.25		14.7	0.411	0.041	1.4		C_0
176	17224.27		13.1	0.431	−0.031	1.4		C_0
177	17240.07		87.1	0.428	−0.226	0.5		C_0
	17257.77		4.2	0.401	0	1.4		A_0
	17260.65		6.8	0.410	0	0.5		A_0
	17266.85		22.2	0.437	0.053	1.4		C_0
	17277.85		26.9	0.396	0.154	0.6		C_0
	17293.18		110.7	0.434	−0.023	0.5		$C_{0,1}$
	17302.29		326.1	0.409	0.024	0.2		$C_{0,1}$
	17313.36		41.0	0.408	−0.074	1.4		C_0
	17333.00							*D*
	17347.40		485.0	0.378	−0.219	0.5		C_0
	17358.61		230.5	0.409	0.184	0.5		C_0
	17372.66		46.3	0.393	0	0.3		A_0
	17386.68		5.8	0.359[a]	0	0.6		A_0
	17417.96		53.4	0.434	−0.058	0.3		*D*
	17434.73		105.4	0.420	−0.041	0.3		$C_{0,1}$
	17464.59		293.9	0.423	−0.044	0.3		$C_{0,1}$
	17477.34		16.5	0.443	0	1.4		A_0
	17500.36		367.4	0.404	−0.030	0.2		$C_{0.1}$
	17510.34		28.0	0.399	0	0.6		A_0
	17526.45		43.0	0.389	0	1.4		A_0
	17540.55		85.3	0.393	−0.067	0.5		C_0
	17548.68		40.7	0.425	0	0.6		A_0
	17554.36		23.9	0.472	0	0.6		A_0
	17557.59		28.1	0.446	0	0.6		A_0
	17561.57		64.7	0.437	0.025	0.5		C_0
	17576.81		198.1	0.441	0	0.3		A_0

(*continued on next page*)

Table 3 (*continued*)

Origin	Origin cold band	Intensity (a.u.)	$\frac{1}{2}(B'+C')$	$\frac{1}{2}(\varepsilon'_{bb}+\varepsilon'_{cc})$	$\Delta(\frac{1}{2}(B'+C'))$ (10^{-3})	X^2A_1 level	Type
17580.85		171.4	0.437	0	0.5		A_0
17607.14		94.3	0.447	0.060	0.5		C_0
17618.24		70.3	0.408	0	0.5		$B_{0,1}$
17630.78		102.5	0.404	0.049	0.6		C_0
17644.83		18.3	0.403	0	0.6		A_0
17661.86		184.0	0.435	0.079	1.8		C_0
17664.78		666.8	0.392	0.072	0.8		C_0
17679.56		222.4	0.434	0.118	2.9		C_0
17682.00							D
17709.74		60.2	0.424	−0.046	0.5		C_0
17711.80		94.8	0.391	0.013	0.5		C_0
17732.20		126.7	0.419	−0.246	0.5		C_0
17744.89		75.2	0.455	−0.048	1.4		C_0
17770.42		90.6	0.433	−0.037	0.4		C_0
17776.25		36.2	0.424	0	0.6		A_0
17788.00							D
17795.00		108.7	0.438	0	0.6		A_0
17802.75		236.7	0.429	0.037	0.5		C_0
17814.48		68.3	0.417	0	0.5		A_0
17825.68		118.3	0.391	−0.073	0.5		C_0
17834.06		30.4	0.420	0	0.5		A_0
17848.98		10.8	0.356[a]	0	0.6		A_0
17854.00							D
17886.86		346.5	0.421	0.076	0.5		C_0
17920.88		59.9	0.418	0	0.5		A_0
17932.57		62.5	0.427	0	0.5		A_0
17948.41		142.0	0.399	−0.029	0.5		C_0

As mentioned before, the ε' parameters for the $K=0$ and $K=1$ stacks are fitted independently, since the levels of the two stacks may be affected differently by vibronic interactions. This procedure has only be applied to this band in view of the high spectral quality of the $K=1$ transitions that is generally lacking in most of the other bands listed in Table 4. This explains the differences for the constants listed for the 14851 cm^{-1} band in Table 6—independent ε values for $K=0$ and $K=1$—and Tables 3 and 4, where the standard procedure—one ε for both $K=0$ and $K=1$—has been applied. From the values of the parameters one may infer that there is vibronic interaction, although from the high intensity of the band one might be tempted to conclude that it has strong $^2B_2$ character with little mixing with the electronic ground state. The latter is also reflected in the increase of rotational constant upon electronic excitation. Whatever the explanation is of the high intensity of the 14851 cm^{-1} band, it can be used to advantage for remote sensing of the $^{15}NO_2$ isotopologue, since there is no interference from nearby bands.

4. Discussion and conclusion

From the previous sections it becomes clear that both the variety in and the number of rovibronic transitions in the X^2A_1–A^2B_2 is impressive. A stick diagram (Fig. 1) shows a clear polyad structure existing in the bright A^2B_2 state and most of the individual bands have been rotationally resolved (Figs. 2–6), but it has not been possible to put vibrational labels to individual bands. As mentioned in Section 1, this is due to the coupling of the ground X^2A_1 and the lowest A^2B_2 electronic states above the conical intersection. Rotational fits, however, have been possible in most of the observed spectra. In Tables 3 and 4 the molecular parameters for the upper state component are summarized for $K=0$ and $K=1$ bands, respectively. Initially we hoped to find a clear relationship between values of the rotational constants and the degree of mixing of the electronic ground state and the first electronically excited state, but this relationship is far from obvious. Clearly most fitted bands—about 150—result in $\frac{1}{2}(B'+C')$ constants that are close to or within 5% of the ground state value and no large geometry change is expected for these bands. This is shown in the histogram in Fig. 7 where the distribution of the $\frac{1}{2}(B'+C')$ values is given. In a limited number of cases, however, a substantial (>5%) increase is observed—e.g., in the case of the strong 14851 cm^{-1} band with a $\frac{1}{2}(B'+C')$ value of 0.47 cm^{-1}. This indicates an upper level with strong A^2B_2 electronic character. Also in a few cases $\frac{1}{2}(B'+C')$ values are found that are substantially smaller than the ground state value. In these cases the bands generally turn out to be weak and the fitted constants should be regarded as effective parameters only.

Table 4
Overview of all fitted $K = 1$ bands in the A^2B_2–X^2A_1 electronic transition of $^{15}NO_2$ in the 14300–18000 cm^{-1} region

	Origin	A'	B'	C'	ε'_{aa}	ε'_{bb}	ε'_{cc}	$\Delta(\frac{1}{2}(B'+C'))$ (10^{-3})
4	14387.76	9.109	0.427	0.349	0.530	−0.037	−0.079	0.7
15	14675.20	10.123	0.469	0.368	0.984	−0.072	−0.146	0.7
HB60	14780.99	7.902	0.449	0.405	0.133	0.030	−0.032	0.6
22	14851.27	7.679	0.482	0.444	−1.133	0.159	0.036	0.3
35	15023.94	8.010	0.457	0.352	0.353	−0.161	0.048	0.5
37	15057.94	7.783	0.446	0.374	0.800	−0.208	0.093	0.7
60	15520.95	7.952	0.458	0.398	0.073	−0.002	−0.003	0.6
68	15647.83	8.989	0.512	0.364	1.834	0.131	−0.134	1.5
75	15732.12	9.350	0.426	0.396	1.551	0.525	−0.527	0.5
85	15919.20	8.627	0.442	0.354	0.609	−0.308	0.367	0.3
HB138	15970.10	8.903	0.514	0.247	1.303	−0.074	−0.253	0.2
HB148	16121.70	8.412	0.483	0.405	−0.965	0.120	0.028	0.9
98	16145.01	7.908	0.445	0.392	−0.108	0.064	0.093	0.9
106	16267.12	7.910	0.454	0.399	0.249	0.105	−0.218	0.4
108	16324.31	6.325	0.519	0.358	−0.666	0.329	−0.141	0.5
113	16416.10	7.621	0.470	0.364	−0.307	0.098	0.028	0.4
115	16435.58	4.514	0.459	0.415	−1.650	0.017	0.184	0.3
121	16512.66	11.601	0.438	0.398	0.402	0.001	0.055	0.6
135	16671.62	8.185	0.447	0.358	0.084	−0.003	−0.000	0.5
148	16861.75	9.025	0.438	0.425	−0.358	−0.008	0.113	0.5
152	16899.85	7.171	0.403	0.401	0.501	−0.045	−0.042	0.5
153	16913.66	6.566	0.491	0.337	0.259	0.362	0.576	0.8
172	17169.70	8.313	0.555	0.213	0.124	−0.134	0.070	0.4
	17293.18	2.469	0.471	0.403	0.085	−0.042	−0.005	0.6
	17302.28	17.366	0.441	0.378	−0.043	0.007	0.041	0.4
	17434.70	4.921	0.474	0.374	0.185	−0.061	−0.020	0.5
	17464.48	5.411	0.546	0.333	−0.143	0.001	−0.060	0.7
	17500.29	6.021	0.519	0.316	0.232	−0.027	−0.034	0.7
	17618.24	11.326	0.441	0.376	0.146	−0.030	0.028	0.6

The numbering of the bands refers to that used in Table 3, where only the $K = 0$ parameters are listed. HB indicates a hot band transition. All values are given in cm^{-1}. $\Delta(\frac{1}{2}(B'+C'))$ $(10^{-3}$ $cm^{-1})$ is a measure for the quality of the fit. Even though this value is rather small, one should regard the majority of the constants listed here as effective parameters only.

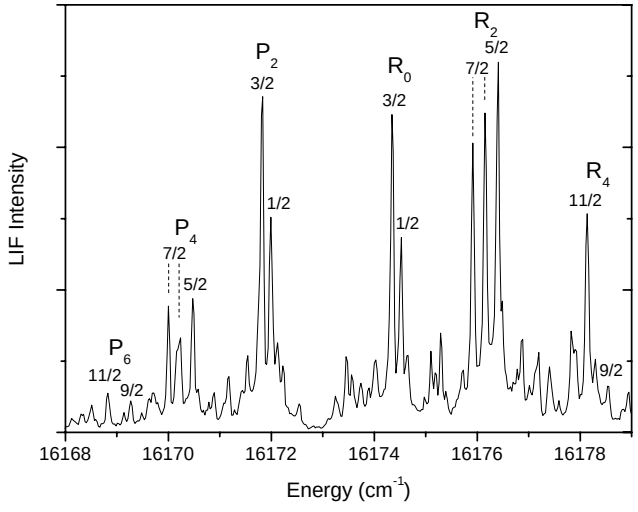

Fig. 5. An example of a perturbed $K = 0$ band in the electronic A^2B_2–X^2A_1 transition of $^{15}NO_2$ with resolved spin splitting. Transitions to $N' = 3$, however, have a triplet structure because of an interaction with a dark state. This example (No. 99 in Table 3) is one of the more regular perturbed states.

Analogously, a low value for the A-constant indicates a strong A^2B_2 electronic character [2]. When A is low (<7 cm^{-1}) and $\frac{1}{2}(B'+C')$ is large (>0.45 cm^{-1}) we can expect a significant A^2B_2 electronic character. From Tables 3 and 4 it becomes clear that only a few bands, e.g., at 16324 and 16435 cm^{-1}, fulfill this criterion and remarkably, these two bands are among the five strongest bands of polyad 9. In general, however, such conclusions cannot be drawn and the value of the rotational constants alone is clearly not sufficient to indicate the degree of vibronic mixing between the X^2A_1 and A^2B_2 state. This frustrates efforts to categorize excited states according to strong or weak vibronic couplings with the aim to guide vibrational assignments. The fine structure constants behave even worse, for that matter, since they are also dependent on the particular rotational state. As for the determination of the degree of mixing of the two lowest electronic states, measuring hyperfine couplings from high resolution spectra seems to be a more preferable approach (see also [7–9]). Unfortunately, the simple relationship between hyperfine constant and degree of mixing of electronic states, is only valid in an energy region of a few thousands of wavenumbers just above the conical intersection [37].

Another approach to learn from the present data set and to compare the spectral features of the $^{15}NO_2$ isotopologue with those of the main isotopologue is by statistical argu-

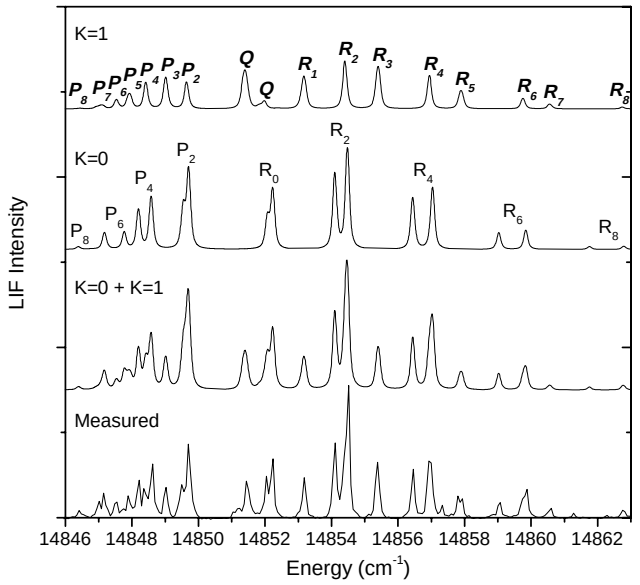

Fig. 6. The rotationally analyzed A^2B_2–X^2A_1 spectrum of the vibronic band of $^{15}NO_2$ at 14851 cm^{-1} (see Table 3, band No. 22, to compare for intensities). Fits for the $K = 0$ and $K = 1$ stacks are shown separately and when added give a nearly perfect simulation of the measured spectrum. Observed and calculated line positions are listed in Table 5. The corresponding constants are listed in Table 6.

ments. The numbers of observed and calculated $^2B_2$ vibronic levels are compared in order to estimate the fraction of (experimentally) missing vibronic levels. The calculated number is derived from a model of integrated density previously checked and used for the $^{14}NO_2$ isotopologue in the same energy range [15,17]. According to this model the smoothed integrated density $N(E)$—including both a_1 and b_2 vibrational symmetries—of the X^2A_1 ground state of $^{14}NO_2$ is well described by a simple polynomial, consisting of two terms:

$$N(E) = a_3 \times (E + E_0)^3 + a_6 \times (E + E_0)^6. \quad (7)$$

The energy E is taken from the vibronic ground state $(0,0,0)$ of the X^2A_1 electronic ground state and E_0 is the ZPE of the ground state which is 1871.05 cm^{-1} for $^{14}NO_2$ and 1841.06 cm^{-1} for $^{15}NO_2$. The first term of $N(E)$ represents the harmonic contribution expected for a 3D oscillator. The second term, which takes into account anharmonic contributions, has been determined empirically by fitting the experimental $N(E)$, including the full set of levels up to 11 500 cm^{-1} [15]. The integrated density of the electronically excited state, A^2B_2, is assumed to obey the same analytic form but with different parameters and with an energy shift that corresponds to an energy difference between the minimum of the A^2B_2 and the minimum of the X^2A_1 potential energy surface.

The ^{15}N versus ^{14}N isotope effect on the a_3 coefficient is easily derived from the isotope effect on the three harmonic frequencies:

$$a_3(^{15}NO_2) = a_3(^{14}NO_2) \times \left(\frac{\omega_1\omega_2\omega_3}{\omega_1^*\omega_2^*\omega_3^*}\right), \quad (8)$$

where ω_1, ω_2, ω_3 and ω_1^*, ω_2^*, ω_3^* are the three harmonic vibrational frequencies of $^{14}NO_2$ and $^{15}NO_2$, respectively. These three X^2A_1 harmonic vibrational frequencies have been calculated for the two isotopologues with the same potential energy surface [38] in order to get the correct isotopologue ratio. Note that the harmonic vibrational frequencies evolve as the inverse of the square root of the masses. In contrast, the isotope effect on the $a_6 * (E + E_0)^6$ anharmonic term is not well characterized. In the studied range the numerical contribution of the anharmonic term is much smaller than the cubic term. According to [39] the Dunham anharmonicities, described by the six (x_{ij}) coefficients $(1 \leqslant i, j \leqslant 3;\ i \geqslant j)$ evolves as the inverse of the mass ratio. This gives for a_6 of $^{15}NO_2$ a value that is derived from a_6 of $^{14}NO_2$ using:

$$a_6(^{15}NO_2) = a_6(^{14}NO_2) \times \left(\frac{\omega_1\omega_2\omega_3}{\omega_1^*\omega_2^*\omega_3^*}\right)^2. \quad (9)$$

The same analytic formula has been used to calculate the contribution of the A^2B_2 excited state to $N(E)$. All parameters used in the $N(E)$ calculation are summarized in Table 7.

The calculated numbers of vibronic levels using Eqs. (7)–(9) include all symmetries, namely the a_1 and b_2 vibrational symmetries of the C_{2v} group for each electronic state. In contrast, the observed vibronic levels are only of $^2B_2$ vibronic symmetry. Due to vibronic interactions between the X^2A_1 and A^2B_2 states the number of observed $^2B_2$ vibronic levels is the sum of two contributions: the X^2A_1 of b_2 vibrational symmetry and the A^2B_2 of a_1 vibrational symmetry. So, it is necessary to split the two $N(E)$ values of the X^2A_1 and A^2B_2 electronic states in two parts corresponding to their respective a_1 and b_2 vibrational symmetries. At high energies, the a_1 and b_2 vibrational densities are similar but in the present range of measurements, their ratio is significantly different from unity. Numerically a formula has been derived [17] which describes the fraction (R) of the a_1 and b_2 vibrational levels as a function of the energy:

$$R(a_1;E) = 0.5 + \left(\frac{C}{E + E_0}\right)^{\alpha} \quad \text{and}$$
$$R(b_2;E) = 0.5 - \left(\frac{C}{E + E_0}\right)^{\alpha}. \quad (10)$$

The sum of the $R(a_1;E)$ and $R(b_2;E)$ is obviously equal to unity. The levels of a_1 vibrational symmetry have an even number of quanta in the anti-symmetric stretch mode (n_3) and those of b_2 vibrational symmetry have an odd value of n_3. Note that the two ratios, $R(a_1;E)$ and $R(b_2;\mathrm{E})$, converge to 0.5 for increasing E. This analytic form of the ratio is valid for the X^2A_1 and A^2B_2 electronic states but with slightly different coefficients which are available from Table III and Fig. 2 of [17]. The density of $^2B_2$ vibronic levels integrated up to E is the sum of the contributions of b_2 levels of the X^2A_1 state and the a_1 levels of the A^2B_2 state:

$$N(^2B_2;E) = N(X\ ^2A_1;E) \times R(b_2;E) + N(A^2B_2;E) \times R(a_1;E). \quad (11)$$

Table 5
Observed and calculated line positions for both the $K=0$ and $K=1$ stacks of the strong 14851 cm^{-1} vibronic band of $^{15}NO_2$

		ν_{obs}	ν_{calc}	Obs. − calc.
$K=0$				
P_8	(15/2)	14847.15	14847.20	−0.05
P_6	(9/2)	14847.15	14847.17	−0.02
P_6	(11/2)	14847.82	14847.76	0.06
P_4	(5/2)	14848.16	14848.19	−0.03
P_4	(7/2)	14848.61	14848.57	0.04
P_2	(1/2)	14849.51	14849.54	−0.03
P_2	(3/2)	14849.70	14849.70	0.00
R_0	(1/2)	14852.05	14852.07	−0.02
R_0	(3/2)	14852.22	14852.23	−0.01
R_2	(5/2)	14854.10	14854.10	0.00
R_2	(7/2)	14854.50	14854.47	0.03
R_4	(9/2)	14856.45	14856.44	0.01
R_4	(11/2)	14856.95	14857.03	−0.08
R_6	(13/2)	14859.04	14859.03	0.01
R_6	(15/2)	14859.85	14859.84	0.01
$K=1$				
P_7	(11/2)	14847.02	14847.04	−0.03
P_7	(13/2)	14847.15	14847.12	0.03
P_6	(9/2)	14847.50	14847.52	−0.02
P_6	(11/2)	14847.52	14847.54	−0.02
P_5	(9/2)	14847.82	14847.94	−0.13
P_4	(5/2)	14848.34	14848.40	−0.07
P_4	(7/2)	14848.34	14848.42	−0.09
P_3	(3/2)	14849.01	14848.99	0.03
P_3	(5/2)	14849.01	14849.03	−0.01
R_1	(3/2)	14853.18	14853.16	0.02
R_1	(5/2)	14853.18	14853.20	−0.02
R_2	(5/2)	14854.50	14854.40	0.10
R_2	(7/2)	14854.50	14854.41	0.08
R_3	(7/2)	14855.38	14855.38	0.00
R_4	(11/2)	14856.95	14856.95	0.00
R_5	(11/2)	14857.81	14857.85	−0.04
R_5	(13/2)	14857.94	14857.92	0.02
R_7	(15/2)	14860.58	14860.51	0.07
R_7	(17/2)	14860.58	14860.61	−0.03

All values are in cm^{-1}.

Table 6
Spectroscopic constants of the strong 14851 cm^{-1} band of $^{15}NO_2$

ν_{bo}		14851.24(1)
$\frac{1}{2}(B'+C')$		0.468(1)
$\frac{1}{2}(B'-C')$		0.019(1)
A'		7.690(10)
$(\varepsilon'_{bb}+\varepsilon'_{cc})/2$	$K=0$	0.1068(1)
$(\varepsilon'_{bb}+\varepsilon'_{cc})/2$	$K=1$	0.007(6)
ε'_{aa}	$K=1$	0.15(6)
$(\varepsilon'_{cc}-\varepsilon'_{bb})/4$	$K=1$	−0.003(4)
D'_N		$1.0(5)\times10^{-4}$

All values are in cm^{-1}. The values between brackets indicate 2σ uncertainties.

The parameters of these analytic functions are given in Table 7 for $^{14}NO_2$ and $^{15}NO_2$. The comparison between the calculated and observed number of $^{15}NO_2$ $^2B_2$ vibronic levels is given in Table 8 for selected energy intervals.

Here it should be noticed that hot bands are extracted from the initial list in order to consider only the vibronic

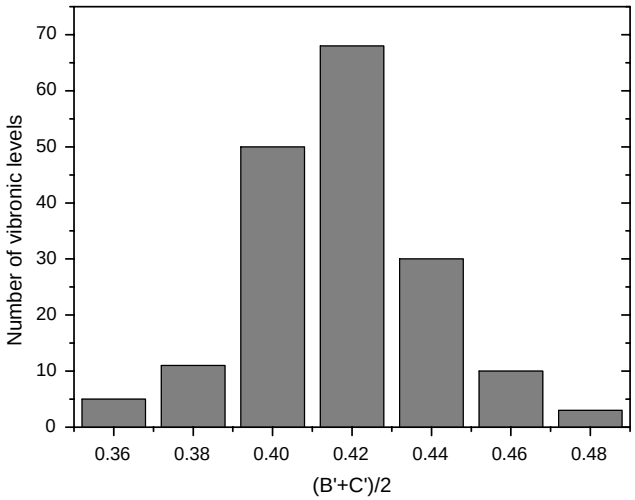

Fig. 7. The histogram shows the distribution of $\frac{1}{2}(B'+C')$ values found for the electronically excited state as listed in Table 3. The gaps are only given for clarity.

Table 7
Parameters used for $^{14}NO_2$ and $^{15}NO_2$ to predict the number of vibronic levels

	$^{14}NO_2$		$^{15}NO_2$	
	X^2A_1	A^2B_2	X^2A_1	A^2B_2
a_3 $(cm^{-1})^{-3}$	1.0696×10^{-10} [a]	1.9×10^{-10} [c]	1.1201×10^{-10} [c]	2.0×10^{-10} [c]
a_6 $(cm^{-1})^{-3}$	4.66×10^{-24} [c]	6.66×10^{-24} [c]	4.75×10^{-24} [c]	7.32×10^{-24} [c]
C (cm^{-1})	1643.11[a]	1151.26[a]	1643.11[a]	1151.26[c]
α	1.197[a]	1.056[a]	1.197[a]	1.056[a]
E_0 (cm^{-1})	1871.05[b]	1843.7[a]	1841.26[a]	1814.3[b]
ΔE (cm^{-1})	0	9733.6[a]	0[a]	9734[c]

[a] From Georges et al. [17].
[b] From Michalski et al. [36].
[c] Estimation.

energies. The fraction of missing levels is significantly larger below 14825 cm^{-1}, mostly because the absorption cross-section of NO_2 decreases to the red. In the range between 14825 to 17250 cm^{-1} the observed levels amount to 68% of the calculated number. In the range above 17250 cm^{-1} cold and hot bands cannot be sorted any more. In this range 48 bands have been observed among which we expect about 4–7 hot bands. This means that the fraction of missing levels is also significantly larger than between 14825 and 17250 cm^{-1}, mostly because the LIF spectrum is denser and more perturbed at high energies [40]. As a consequence the analysis of the statistical properties of vibronic energies and intensities is performed only between 14825 and 17250 cm^{-1}. In this frequency range 159 $^2B_2$ vibronic levels have been observed while 233 $^2B_2$ vibronic levels (180 of X^2A_1 and 53 of A^2B_2) are predicted by the model. This means that 68% of the $^2B_2$ levels has been observed (or 32% of the levels is missing). The number of observed and calculated $^2B_2$ levels in the same energy range of the main isotopologue, $^{14}NO_2$, amounts to 160 and 221, respectively, and the corresponding ratio is 72.5%, comparable to the results presented here for the $^{15}NO_2$ isotopologue.

Table 8
Comparison between calculated and observed vibronic levels of $^{15}NO_2$ $^2B_2$ symmetry in various energy ranges

Energy range	$N_{cal}(X^2A_1,b_2)$	$N_{cal}(A^2B_2,a_1)$	$N_{cal}(^2B_2)$	$N_{exp}(^2B_2)$
14250–14825	32.7	8.3	41	18 (44%)
14825–15425	37.8	10.3	48.1	35 (73%)
15425–16025	41.9	12.1	54.0	38 (70%)
16025–16625	46.5	14.0	60.5	39 (65%)
16625–17250	51.7	16.3	68.0	44 (65%)
14825–17250	**180**	**53**	**233**	**159 (68%)**
17250–17950[a]	67.2	22	89.2	48[b] (54%)

The bold line is highlighted as being the most important result.
[a] The hot bands cannot be discriminated in this range of 700 cm^{-1}.
[b] This number includes a few (most likely between 4 and 7) hot bands.

The distribution of measured LIF intensities has been compared with a Porter–Thomas distribution which is typical for a chaotic system. As the limited S/N ratios prohibit an unambiguous identification of the weaker bands, an experimental threshold is defined in the Porter–Thomas distribution which allows an estimate of the fraction of missing levels. This fraction is about 30% when the intensity modulation—that originates from the polyad structure—is taken into account. This result is in agreement with the fraction of 68% of observed levels determined before from $N(E)$. The next neighbor distribution (NND) is a measurement of the "level repulsion" which is a measure for the strength of vibronic interaction. In order to deal with dimensionless spacings, the energy spectrum is "unfolded" and the energy spacings are normalized to unity [41]. As a result, σ, the second moment of the NND for the set of 159 vibronic levels is $\sigma = 0.69$. This value is significantly higher than $\sigma = 0.53$, the value expected for a fully chaotic system but significantly lower than $\sigma = 1.0$, the value of a random (Poisson like) distribution. From numerical estimations a value $\sigma \cong 0.6$ is expected, when no levels are missing. This means that significant level repulsion is present within the vibronic levels of $^{15}NO_2$ in the 14825–17250 cm^{-1} energy range. This σ value is also close to the value measured for the $^{14}NO_2$ isotopologue. Similarly, the distribution of the $\frac{1}{2}(B' + C')$ rotational constants derived for the $^{15}NO_2$ isotopologue has the same average and the same width as the one found for the $^{14}NO_2$ isotopologue [42]. When comparing $^{15}NO_2$ and $^{14}NO_2$, the expected decrease of $\frac{1}{2}(B' + C')$ due to the increase of the reduced mass is significantly smaller than the width of the distribution.

In summary, the overall average properties of the $^{15}NO_2$ spectrum in the studied range are rather close to those of the $^{14}NO_2$ main isotopologue. The envelopes of the room temperature absorption cross-sections of these two isotopologues are resembling [43]. The polyad structure is present in the spectra of both species with a spacing of ≈720 and ≈715 cm^{-1} for $^{14}NO_2$ and $^{15}NO_2$, respectively. In contrast, the inner structures of the corresponding polyads seem to be completely different for the two isotopologues. For example, the seventh polyad of $^{15}NO_2$, around 14800 cm^{-1}, displays a single very dominant vibronic band at 14851 cm^{-1} (see Section 3.5). This band carries almost half of the total intensity of the seventh polyad. The same polyad of $^{14}NO_2$, on the contrary, displays several vibronic bands with comparable intensities whereas the third and the fifth polyad are also dominated by a single strong band. Our tentative interpretation of these observations is the following: in each polyad the zero order bright character is located in a very few zero order A^2B_2 vibronic levels. According to Frank–Condon calculations performed for the main isotopologue, the two dominant bright levels are the $(0, n_2, 0)$ and $(1, n_2 - 2, 0)$ vibrational A^2B_2 excitations where n_2 is the bending quantum number and that both belong to the same polyad number $n_2 + 1$. These zero order levels interact with a dense set of X^2A_1 levels that are shifted and scrambled by isotope substitution. As a result, in most of the polyads the bright character is distributed among several vibronic eigenstates but in a few polyads the bright character remains located in a few eigenstates. A comparison of the polyad structure observed in room temperature absorption spectra of six isotopologues is in progress [43]. As various isotopologues of NO_2 share the same potential energy surface, we expect to learn more about the conical intersection through the comparison of spectra of different isotopologues. Of special interest will be the difference between symmetric and asymmetric isotopologues, resulting in symmetry forbidden or allowed vibronic transitions. In addition, asymmetric isotopologues have rotational spectra twice as dense as the symmetric ones. Work is currently in progress to classify the asymmetric $^{16}O^{14}N^{18}O$ isotopologue [44].

Acknowledgments

The Netherlands Organization for Scientific Research (NWO) and the Dutch organization for Fundamental Research (FOM) through the MAP program are acknowledged for financial support. R.J. who belongs to ENSPG-INP Grenoble, acknowledges EU support for several visits to the Laser Center Vrije Universiteit within the integrating infrastructure initiative: contract RII3-CT-2003-506350. We thank Bas van Stralen for help in the data analysis.

References

[1] M. Joyeux, R. Jost, M. Lombardi, J. Chem. Phys. 119 (2003) 5923–5932.
[2] R. Jost, M. Garcia Vergniory, A. Campargue, J. Chem. Phys. 119 (2003) 2590–2595.
[3] V. Kurkal, P. Fleurat-Lessard, R. Schinke, J. Chem. Phys. 119 (2003) 1489–1501.
[4] S. Heilliette, A. Delon, D. Reignier, T. Stoecklin, J.C. Rayez, Phys. Chem. Chem. Phys. 5 (2003) 2039–2046.
[5] J. Orphal, S. Dreher, S. Voigt, J.P. Burrows, R. Jost, A. Delon, J. Chem. Phys. 109 (1998) 10217–10221.
[6] R. Jost, M. Joyeux, M. Jacon, Chem. Phys. 283 (2002) 17–28.
[7] C.A. Biesheuvel, J. Bulthuis, M.H.M. Janssen, S. Stolte, J.G. Snijders, J. Chem. Phys. 112 (2000) 3633–3642.
[8] C.A. Biesheuvel, J. Bulthuis, M.H.M. Janssen, J.G. Snijders, S. Stolte, J. Chem. Phys. 109 (1998) 9701–9712.
[9] C.A. Biesheuvel, Ph.D. Thesis, Vrije Universiteit, Amsterdam.
[10] A. Delon, R. Jost, M. Jacon, J. Chem. Phys. 114 (2001) 331–344.
[11] J. Liévin, A. Delon, R. Jost, J. Chem. Phys. 108 (1998) 8931–8943.
[12] B. Kirmse, A. Delon, R. Jost, J. Chem. Phys. 108 (1998) 6638–6651.
[13] A. Delon, R. Georges, B. Kirmse, R. Jost, Faraday Discuss. 102 (1995) 117–128.
[14] D.K. Hsu, D.L. Monts, R. Zare, Spectral Atlas of Nitrogen Dioxide, Academic Press, New York, 1987.
[15] R. Georges, A. Delon, F. Bylicki, R. Jost, A. Campargue, A. Charvat, M. Chenevier, F. Stoeckel, Chem. Phys. 190 (1995) 207–229.
[16] D. Romanini, P. Dupré, R. Jost, Vib. Spectrosc. 19 (1999) 93–106.
[17] R. Georges, A. Delon, R. Jost, J. Chem. Phys. 103 (1995) 1732–1747.
[18] M.D. Olman, C.D. Hause, J. Mol. Spectrosc. 26 (1968) 241–253.
[19] R.E. Blank, C.D. Hause, J. Mol. Spectrosc. 34 (1970) 478–486.
[20] Y. Hamada, J. Mol. Struct. 242 (1991) 367–377.
[21] N. Tanaka, Y. Hamada, C. Yamada, E. Hirota, J. Mol. Spectrosc. 131 (1988) 44–52.
[22] E.A. Volkers, A. Vredenborg, H. Linnartz, J. Bulthuis, S. Stolte, R. Jost, Chem. Phys. Lett. 391 (2004) 106–111.
[23] A. Pedler, F.H. Pollard, in: T. Moeller (Ed.), Inorganic Syntheses, vol. V, McGraw-Hill, New York, 1957, p. 87.
[24] J. Orphal, A. Perrin, J.-M. Flaud, M. Smirnov, S. Himmelmann, S. Voigt, J.P. Burrows, J. Mol. Spectrosc. 204 (2000) 72–79.
[25] C.H. Townes, A.L. Schawlow, Microwave Spectroscopy, Dover, New York, 1975.
[26] C.C. Lin, Phys. Rev. 116 (1959) 903–910.
[27] I.C. Bowater, J.M. Brown, A. Carrington, Proc. R. Soc. Lond. A 333 (1973) 265–288.
[28] R.L. Sams, W.J. Lafferty, J. Mol. Spectrosc. 56 (1975) 399–410.
[29] A. Cabana, M. Laurin, W.J. Lafferty, R.L. Sams, Can. J. Phys. 53 (1975) 1902–1926.
[30] W.C. Bowman, F.C. De Lucia, J. Chem. Phys. 77 (1982) 92–107.
[31] H.J. Vedder, M. Schwartz, H.-J. Foth, W. Demtröder, J. Mol. Spectrosc. 97 (1983) 92–116.
[32] S. Beirle, U. Platt, M. Wenig, T. Wagner, Atm. Chem. Phys. 4 (2004) 1913–1924.
[33] C.E. Sioris, T.P. Kurosu, R.V. Martin, K. Chance, Adv. Space Res. 34 (2004) 780–785.
[34] K. Mauersberger, B. Erbacher, D. Krankowsky, J. Guenter, R. Nickel, Science 283 (1999) 370–372.
[35] H. Umemoto, K. Tanka, S. Oguro, R. Ozeki, M. Ueda, Chem. Phys. Lett. 345 (2001) 44–50.
[36] G. Michalski, R. Jost, D. Sugny, M. Joyeux, M. Thiemens, J. Chem. Phys. 121 (2004) 7153–7161.
[37] J. Xin, S.A. Reid, F. Santoro, C. Petrolongo, J. Chem. Phys. 115 (2001) 8868–8875.
[38] J.L. Hardwick, J.C.D. Brand, Chem. Phys. Lett. 21 (1973) 458–461.
[39] G. Herzberg, Molecular Spectra and Molecular Structure III—Polyatomic Molecules, Van Nostrand Reinhold, New York, 1966.
[40] A. Delon, R. Georges, R. Jost, J. Chem. Phys. 103 (1995) 7740–7772.
[41] T.A. Brody, J. Flores, J.B. French, P.A. Mello, A. Pandey, S.S.M. Wong, Rev. Mod. Phys. 53 (1981) 385–479.
[42] A. Delon, R. Jost, M. Lombardi, J. Chem. Phys. 95 (1991) 5701–5718.
[43] S. Fally, M. Carleer, C. Hermans, A.C. Vandaele, G. Michalski, R. Jost, Proceedings of the 7th Atmospheric Spectroscopic Applications (ASA) meeting, Reims, France, 2005.
[44] E.A. Volkers, H. Linnartz, J. Bulthuis, S. Stolte, R. Jost, 2005 (in preparation).